IN-34
176741
P36

NASA Technical Memorandum 106266
ICOMP-93-25

Viscous Analysis of Three-Dimensional Rotor Flows Using a Multigrid Method

A. Arnone
Institute for Computational Mechanics in Propulsion
Lewis Research Center
Cleveland, Ohio

and *University of Florence*
Florence, Italy

(NASA-TM-106266) VISCOUS ANALYSIS OF THREE-DIMENSIONAL ROTOR FLOWS USING A MULTIGRID METHOD (NASA) 36 p

N94-11481

Unclas

G3/34 0176741

July 1993

VISCOUS ANALYSIS OF THREE-DIMENSIONAL ROTOR FLOWS USING A MULTIGRID METHOD

A. Arnone [†]

Department of Energy Engineering
University of Florence
Florence, Italy

and

Institute for Computational Mechanics in Propulsion
Lewis Research Center
Cleveland, Ohio

ABSTRACT

A three-dimensional code for rotating blade-row flow analysis has been developed. The space discretization uses a cell-centered scheme with eigenvalues scaling for the artificial dissipation. The computational efficiency of a four-stage Runge-Kutta scheme is enhanced by using variable coefficients, implicit residual smoothing, and a full-multigrid method.

An application is presented for the NASA rotor 67 transonic fan. Due to the blade stagger and twist, a zonal, non-periodic H-type grid is used to minimize the mesh skewness. The calculation is validated by comparing it with experiments in the range from the maximum flow rate to a near-stall condition. A detailed study of the flow structure near peak efficiency and near stall is presented by means of pressure distribution and particle traces inside boundary layers.

[†] *Assistant Professor*

INTRODUCTION

In the last decade Fluid Dynamics has undergone impressive evolution both in the understanding and in the simulation of flow features. In this process, Computational Fluid Dynamics (CFD) is playing a more and more important role. Modern turbomachinery operates under very complex three-dimensional flow conditions, and further improvement requires detailed knowledge of the flow structure. Particularly, the need to estimate off-design conditions, secondary flows, and heat transfer forces us to look at viscous models. The real flow inside a turbomachine is unsteady and strongly influenced by rotor-stator interactions, wake, and clearance effects. Even if some important steps have been made in the time-accurate and time-averaged simulation of entire stages (e.g. Rai, 1987, Rao and Delaney, 1990, Adamczyk et al., 1990), a steady blade-row analysis should still be considered a basic tool for modern design. The works of Subramanian and Bozzola (1987), Chima and Yokota (1988), Choi and Knight (1988), Davis et al. (1988), Hah (1989), Nakahashi et al. (1989), Weber and Delaney (1991), and Dawes (1991) are some important steps in the prediction of three-dimensional viscous cascade flows.

In 1988, the University of Florence started a joint project with NASA (ICASE and ICOMP) on viscous cascade flow simulation. During this research project, the TRAF2D and TRAF3D codes (TRAnsonic Flow 2D/3D) were developed (Arnone et al. 1988, 1991, 1992). Those codes are capable of solving viscous cascade flows using H-type or C-type grids and of predicting heat transfer effects. In the present work, the procedure was extended to the case of rotating blade passages. Particular attention has been dedicated to important aspects such as minimization of the grid skewness, accuracy, and computational cost.

As for accuracy, non-periodic C- or H-type grids are stacked in three dimensions. The removal of periodicity allows the grid to be only slightly distorted even for cascades having a large camber or a high stagger angle and twist. This allows us to pick up details of the throat flow with a reasonable number of grid points. A very low level of artificial dissipation is guaranteed by eigenvalues scaling, which is a three-dimensional extension of the one proposed by Swanson and Turkel (1987), and Martinelli and Jameson (1988).

The two-layer eddy-viscosity model of Baldwin and Lomax (1978) is used for the turbulence closure.

As for efficiency, the Reynolds-averaged Navier-Stokes equations are solved using a Runge-Kutta scheme in conjunction with accelerating techniques. Variable-coefficient implicit residual smoothing, as well as the Full-Approximation-Storage multigrid scheme of Brandt (1979) and Jameson (1983) are used in the TRAF3D code. Those accelerating strategies are implemented in conjunction with grid refinement to get a Full Multigrid Method.

The code is validated by studying the NASA rotor 67 transonic fan. This fan has important viscous and three-dimensional effects and experiments are available in a wide range of flow rates from the maximum one to near stall. Moreover, this geometry was recently proposed as an AGARD test case for code validation (Fottner, 1990) and calculations from several authors are available for discussion.

By using the accelerating strategies, accurate, viscous 3D solutions can be obtained in about half an hour on a modern supercomputer such as a Cray Y-MP.

GOVERNING EQUATIONS

Let ρ, u, v, w, p, T, E, and H denote respectively density, the absolute velocity components in the x, y, and z Cartesian directions, pressure, temperature, specific total energy, and specific total enthalpy. The three-dimensional, unsteady, Reynolds-averaged Navier-Stokes equations can be written for a rotating blade passage in conservative form in a curvilinear coordinate system ξ, η, ζ as,

$$\frac{\partial\left(J^{-1}Q\right)}{\partial t}+\frac{\partial F}{\partial \xi}+\frac{\partial G}{\partial \eta}+\frac{\partial H}{\partial \zeta}=\frac{\partial F_v}{\partial \xi}+\frac{\partial G_v}{\partial \eta}+\frac{\partial H_v}{\partial \zeta}+I \qquad (1)$$

where the Cartesian system x,y,z is rotating with angular velocity Ω around the x axis,

$$Q=\left\{\begin{matrix}\rho \\ \rho u \\ \rho v \\ \rho w \\ \rho E\end{matrix}\right\},\quad F=J^{-1}\left\{\begin{matrix}\rho U \\ \rho u U+\xi_x p \\ \rho v U+\xi_y p \\ \rho w U+\xi_z p \\ \rho H U+\xi_t p\end{matrix}\right\},\quad G=J^{-1}\left\{\begin{matrix}\rho V \\ \rho u V+\eta_x p \\ \rho v V+\eta_y p \\ \rho w V+\eta_z p \\ \rho H V-\eta_t p\end{matrix}\right\} \qquad (2a)$$

$$H=J^{-1}\left\{\begin{matrix}\rho W \\ \rho u W+\zeta_x p \\ \rho v W+\zeta_y p \\ \rho w W+\zeta_z p \\ \rho H W+\zeta_t p\end{matrix}\right\},\quad I=\left\{\begin{matrix}0 \\ 0 \\ \rho\Omega w \\ -\rho\Omega v \\ 0\end{matrix}\right\} \qquad (2b)$$

The contravariant velocity components of eqs. (2) are written as,

$$U=\xi_t+\xi_x u+\xi_y v+\xi_z w$$

$$
\begin{aligned}
V &= \eta_t + \eta_x u + \eta_y v + \eta_z w \\
W &= \zeta_t + \zeta_x u + \zeta_y v + \zeta_z w
\end{aligned}
\tag{3}
$$

and the transformation metrics are defined by,

$$
\begin{gathered}
\xi_x = J(y_\eta z_\zeta - y_\zeta z_\eta), \quad \xi_y = J(z_\eta x_\zeta - z_\zeta x_\eta) \\
\xi_z = J(x_\eta y_\zeta - x_\zeta y_\eta), \quad \eta_x = J(y_\zeta z_\xi - y_\xi z_\zeta) \\
\eta_y = J(z_\zeta x_\xi - z_\xi x_\zeta), \quad \eta_x = J(x_\zeta y_\xi - x_\xi y_\zeta) \\
\zeta_x = J(y_\xi z_\eta - z_\xi y_\eta), \quad \zeta_y = J(z_\xi x_\eta - x_\xi z_\eta) \\
\zeta_z = J(x_\xi y_\eta - y_\xi x_\eta), \quad \xi_t = -x_t \xi_x - y_t \xi_y - z_t \xi_z \\
\eta_t = -x_t \eta_x - y_t \eta_y - z_t \eta_z, \quad \zeta_t = -x_t \zeta_x - y_t \zeta_y - z_t \zeta_z \\
x_t = 0, \quad y_t = -\Omega z, \quad z_t = \Omega y
\end{gathered}
\tag{4}
$$

where the Jacobian of the transformation J is,

$$
J^{-1} = x_\xi y_\eta z_\zeta + x_\eta y_\zeta z_\xi + x_\zeta y_\xi z_\eta - x_\xi y_\zeta z_\eta - x_\eta y_\xi z_\zeta - x_\zeta y_\eta z_\xi \tag{5}
$$

The viscous flux terms are assembled in the form,

$$
F_v = J^{-1} \begin{Bmatrix} 0 \\ \xi_x \tau_{xx} + \xi_y \tau_{xy} + \xi_z \tau_{xz} \\ \xi_x \tau_{yx} + \xi_y \tau_{yy} + \xi_z \tau_{yz} \\ \xi_x \tau_{zx} + \xi_y \tau_{zy} + \xi_z \tau_{zz} \\ \xi_x \beta_x + \xi_y \beta_y + \xi_z \beta_z \end{Bmatrix}
$$

$$G_v = J^{-1} \left\{ \begin{matrix} 0 \\ \eta_x \tau_{xx} + \eta_y \tau_{xy} + \eta_z \tau_{xz} \\ \eta_x \tau_{yx} + \eta_y \tau_{yy} + \eta_z \tau_{yz} \\ \eta_x \tau_{zx} + \eta_y \tau_{zy} + \eta_z \tau_{zz} \\ \eta_x \beta_x + \eta_y \beta_y + \eta_z \beta_z \end{matrix} \right\} \tag{6}$$

$$H_v = J^{-1} \left\{ \begin{matrix} 0 \\ \zeta_x \tau_{xx} + \zeta_y \tau_{xy} + \zeta_z \tau_{xz} \\ \zeta_x \tau_{yx} + \zeta_y \tau_{yy} + \zeta_z \tau_{yz} \\ \zeta_x \tau_{zx} + \zeta_y \tau_{zy} + \zeta_z \tau_{zz} \\ \zeta_x \beta_x + \zeta_y \beta_y + \zeta_z \beta_z \end{matrix} \right\}$$

where,

$$\begin{aligned} \tau_{xx} &= 2\mu u_x + \lambda(u_x + v_y + w_z) \\ \tau_{yy} &= 2\mu v_y + \lambda(u_x + v_y + w_z) \\ \tau_{zz} &= 2\mu w_z + \lambda(u_x + v_y + w_z) \\ \tau_{xy} = \tau_{yx} &= \mu(u_y + v_x) \\ \tau_{xz} = \tau_{zx} &= \mu(u_z + w_x) \\ \tau_{yz} = \tau_{zy} &= \mu(v_z + w_y) \\ \beta_x &= u\,\tau_{xx} + v\,\tau_{xy} + w\,\tau_{xz} + k\,T_x \\ \beta_y &= u\,\tau_{yx} + v\,\tau_{yy} + w\,\tau_{yz} + k\,T_y \\ \beta_z &= u\,\tau_{zx} + v\,\tau_{zy} + w\,\tau_{zz} + k\,T_z \end{aligned} \tag{7}$$

and the Cartesian derivatives of (7) are expressed in terms of ξ-, η-, and ζ-derivatives using the chain rule, *i.e.*,

$$u_x = \xi_x u_\xi + \eta_x u_\eta + \zeta_x u_\zeta \tag{8}$$

The pressure is obtained from the equation of state,

$$p = \rho RT \tag{9}$$

According to the Stokes hypothesis, λ is taken to be $-2\mu/3$ and a power law is used to determine the molecular coefficient of viscosity μ as function of temperature. The eddy-viscosity hypothesis is used to account for the effect of turbulence. The molecular viscosity μ and the molecular thermal conductivity k are replaced with,

$$\mu = \mu_l + \mu_t \tag{10}$$

$$k = c_p\left[\left(\frac{\mu}{Pr}\right)_l + \left(\frac{\mu}{Pr}\right)_t\right] \tag{11}$$

where c_p is the specific heat at constant pressure, Pr is the Prandtl number, and the subscripts l and t refer to laminar and turbulent respectively. The turbulent quantities μ_t and Pr_t are computed using the two-layer mixing length model of Baldwin and Lomax (1978). The contribution of the eddy viscosity is computed separately in the blade-to-blade direction η and in the spanwise direction ζ. The inverse of the square of the wall distances d is then used to compute the resulting eddy viscosity,

$$f = \frac{\dfrac{1}{d_\eta^2}}{\left(\dfrac{1}{d_\eta^2} + \dfrac{1}{d_\zeta^2}\right)} \tag{12}$$

$$\mu_t = f\left(\mu_t\right)_\eta + \left(1 - f\right)\left(\mu_t\right)_\zeta \tag{13}$$

The transitional criteria of Baldwin and Lomax is adopted on the airfoil surface while on the end walls, the shear layer is assumed to be fully-turbulent from the inlet boundary.

SPATIAL DISCRETIZATION

Traditionally, using a finite-volume approach, the governing equations are discretized in space starting from an integral formulation and without any intermediate mapping (e.g. Jameson at al., 1981, Ni, 1981, Holmes and Tong, 1985). The transformation metrics of (4) can be then associated with the projections of the face areas as the contravariant components of (3) can be related to the normal components of the relative velocity. In the present work, due to the large use of eigenvalues and curvilinear quantities, we found it more convenient to map the Cartesian space (x,y,z) in a generalized curvilinear one (ξ, η, ζ). In the curvilinear system, the equation of motion (1) can be easily rewritten in integral form by means of Green's theorem and the metric terms are handled following the standard finite-volume formulation. The computational domain is divided into hexahedrons and the transformation metrics are evaluated so that the projected areas of the cell-faces are given by the ratio of the appropriate metric derivatives to the Jacobian ones, *i.e.* ξ_x/J is the projection onto the x-axis of a cell face at a fixed ξ location. A cell-centered scheme is used to store the flow variables. On each cell face the convective and diffusive fluxes are calculated after computing the necessary flow quantities at the face center. Those quantities are obtained by a simple averaging of adjacent cell-center values of the dependent variables.

BOUNDARY CONDITIONS

In cascade calculations we have four different types of boundaries: inlet, outlet, solid walls, and periodicity. At the inlet, the presence of boundary layers, on hub and tip end walls, is accounted for by giving a total pressure and a total temperature profile whose distribution simulates the experimental one. According to the theory of characteristics, the flow angles, total pressure, total temperature, and isentropic relations are used at the subsonic-axial inlet, while the outgoing Riemann invariant is taken from the interior. At the subsonic-axial outlet, the average value of the static pressure at the hub is prescribed and the density and components of velocity are extrapolated together with the circumferential distribution of pressure. The radial equilibrium equation is used to determine the spanwise distribution of the static pressure. On the solid walls, the pressure is extrapolated from the interior points, and the no-slip condition and the temperature condition are used to compute density and total energy. For the calculations presented in this paper, all the walls have been assumed to be at a constant temperature equal to the total inlet one.

Cell-centered schemes are generally implemented using phantom cells to handle the boundaries. The periodicity from blade passage to blade passage is, therefore, easily overimposed by setting periodic phantom cell values. On the boundaries where the grid is not periodic, the phantom cells overlap the real ones. Linear interpolations are then used to compute the value of the dependent variables in phantom cells. Even if this approach does not guarantee conservation of mass, momentum, and energy, no accuracy losses have been experienced unless strong flow gradients occur along non-periodic grid boundaries with strong differences in mesh size. In the present work, the number of fine cells to be used for interpolation on a coarse cell never exceeded three.

The clearance region is handled by imposing periodicity conditions across the airfoil without any modellization of the blade cross-section.

ARTIFICIAL DISSIPATION

In viscous calculations, dissipating properties are present due to diffusive terms. Away from the shear layer regions, the physical diffusion is generally not sufficient to prevent the odd-even point decoupling of centered schemes. Thus, to maintain stability and to prevent oscillations near shocks or stagnation points, artificial dissipation terms are also included in the viscous calculations. Equation (1) is written in semi-discrete form as,

$$\frac{\partial Q}{\partial t} + C(Q) - D(Q) = 0 \tag{14}$$

where the discrete operator C accounts for the physical convective and diffusive terms, while D is the operator for the artificial dissipation. The artificial dissipation model used in this paper is basically the one originally introduced by Jameson, Schmidt, and Turkel (1981). In order to minimize the amount of artificial diffusion inside the shear layer, the eigenvalues scaling of Martinelli and Jameson (1988), and Swanson and Turkel (1987) have been used to weight these terms. The quantity $D(Q)$ in eq. (14) is defined as,

$$D(Q) = \left(D_\xi^2 - D_\xi^4 + D_\eta^2 - D_\eta^4 + D_\zeta^2 - D_\zeta^4\right)Q \tag{15}$$

where, for example, in the ξ curvilinear coordinates we have,

$$\begin{aligned} D_\xi^2 Q &= \nabla_\xi\left(\Lambda_{i+1/2,j,k}\, \varepsilon^{(2)}_{i+1/2,j,k}\right) \Delta_\xi Q_{i,j,k} \\ D_\xi^4 Q &= \nabla_\xi\left(\Lambda_{i+1/2,j,k}\, \varepsilon^{(4)}_{i+1/2,j,k}\right) \Delta_\xi \nabla_\xi \Delta_\xi Q_{i,j,k} \end{aligned} \tag{16}$$

i,j,k are indices associated with the ξ,η,ζ directions and ∇_ξ, Δ_ξ are forward and backward difference operators in the ξ direction. The variable scaling factor Λ is defined for the three-dimensional case as,

$$\Lambda_{i+1/2,j,k} = \frac{1}{2}\left[\left(\Lambda_\xi\right)_{i,j,k} + \left(\Lambda_\xi\right)_{i+1,j,k}\right] \tag{17}$$

where,

$$\Lambda_\xi = \Phi_\xi \lambda_\xi \tag{18}$$

The definition of the coefficient Φ has been extended to the three-dimensional case as follows,

$$\Phi_\xi = 1 + \left(\frac{\lambda_\eta}{\lambda_\xi}\right)^\sigma + \left(\frac{\lambda_\zeta}{\lambda_\xi}\right)^\sigma$$

$$\Phi_\eta = 1 + \left(\frac{\lambda_\xi}{\lambda_\eta}\right)^\sigma + \left(\frac{\lambda_\zeta}{\lambda_\eta}\right)^\sigma \tag{19}$$

$$\Phi_\zeta = 1 + \left(\frac{\lambda_\xi}{\lambda_\zeta}\right)^\sigma + \left(\frac{\lambda_\eta}{\lambda_\zeta}\right)^\sigma$$

where λ_ξ, λ_η, and λ_ζ are the scaled spectral radii of the flux Jacobian matrices for the convective terms,

$$\begin{aligned} \lambda_\xi &= |U| + a\sqrt{\xi_x^2 + \xi_y^2 + \xi_z^2} \\ \lambda_\eta &= |V| + a\sqrt{\eta_x^2 + \eta_y^2 + \eta_z^2} \\ \lambda_\zeta &= |W| + a\sqrt{\zeta_x^2 + \zeta_y^2 + \zeta_z^2} \end{aligned} \tag{20}$$

and a is the speed of sound. Note that the effect of the grid rotation is accounted for in (20) through the definition of the contravariant components of velocities of (3). The exponent σ is generally defined by $0<\sigma \leq 1$, and for two-dimensional applications, a value of $2/3$ gives satisfactory results. In three-dimensional cascade flow calculations, we generally have highly stretched meshes in two directions near corners. We found that $\sigma = 0.4$ introduces enough scaling without compromising the robustness. The coefficients $\varepsilon^{(2)}$ and $\varepsilon^{(4)}$ use the pressure as a sensor for shocks and stagnation points, and are defined as follows,

$$\varepsilon^{(2)}_{i+1/2,j,k} = k^{(2)} MAX(\nu_{i-1,j,k}, \nu_{i,j,k}, \nu_{i+1,j,k}, \nu_{i+2,j,k}) \tag{21}$$

$$\nu_{i,j,k} = \left| \frac{p_{i-1,j,k} - 2p_{i,j,k} + p_{i+1,j,k}}{p_{i-1,j,k} + 2p_{i,j,k} + p_{i+1,j,k}} \right| \tag{22}$$

$$\varepsilon^{(4)}_{i+1/2,j,k} = MAX\left[0,\left(K^{(4)} - \varepsilon^{(2)}_{i+1/2,j,k}\right)\right] \tag{23}$$

where typical values for the constants $K^{(2)}$ and $K^{(4)}$ are *1/2* and *1/64* respectively. For the remaining directions η and ζ, the contribution of dissipation is defined in a similar way. The computation of the dissipating terms is carried out in each coordinate direction as the difference between first and third difference operators. Those operators are set to zero on solid walls in order to reduce the global error on the conservation property and to prevent the presence of undamped modes (Pulliam, 1986, and Swanson and Turkel, 1988,).

It is important to anticipate now that from the definition of residual of (25), variable scaling, and time steps of (26,27,28), it results that the artificial dissipation is scaled with a factor proportional to the ratio between the global time step and the inviscid time step. Close to solid walls, the grid volume is very small and viscous time step limitation is dominant. The ratio of the time step over the inviscid one becomes very small and most of the artificial dissipation is removed.

TIME-STEPPING SCHEME

The system of the differential equation (14) is advanced in time using an explicit four stage Runge-Kutta scheme until the steady-state solution is reached . A hybrid scheme is implemented, where, for economy, the viscous terms are evaluated only at the first stage and then frozen for the remaining stages. If *n* is the index associated with time we will write it in the form,

$$\begin{aligned} Q^{(0)} &= Q^{n} \\ Q^{(1)} &= Q^{(0)} + \alpha_1 R\left(Q^{(0)}\right) \\ Q^{(2)} &= Q^{(0)} + \alpha_2 R\left(Q^{(1)}\right) \\ Q^{(3)} &= Q^{(0)} + \alpha_3 R\left(Q^{(2)}\right) \\ Q^{(4)} &= Q^{(0)} + \alpha_4 R\left(Q^{(3)}\right) \\ Q^{n+1} &= Q^{(4)} \end{aligned} \tag{24}$$

$$\alpha_1 = \frac{1}{4}, \quad \alpha_2 = \frac{1}{3}, \quad \alpha_3 = \frac{1}{2}, \quad \alpha_4 = 1$$

where the residual $R\ (Q)$ is defined by,

$$R(Q) = \Delta t\, J\left[C(Q) - D(Q)\right] \tag{25}$$

Good, high-frequency damping properties, important for the multigrid process, have been obtained by performing two evaluations of the artificial dissipating terms, at the first and second stages. It is worthwhile to notice that, in the Runge-Kutta time-stepping schemes, the steady state solution is independent of the time step; therefore, this stepping is particularly amenable to convergence acceleration techniques.

ACCELERATION TECHNIQUES

In order to reduce the computational cost, four techniques are employed to speed up convergence to the steady state-solution. These techniques: 1) local time-stepping; 2) residual smoothing; 3) multigrid; 4) grid refinement; are separately described in the following.

Local Time-Stepping

For steady state calculations with a time-marching approach, a faster expulsion of disturbances can be achieved by locally using the maximum available time step. In the present work the local time step limit Δt is computed accounting for both the convective (Δt_c) and diffusive (Δt_d) contributions as follows,

$$\Delta t = c_0 \left(\frac{\Delta t_c \Delta t_d}{\Delta t_c + \Delta t_d} \right) \tag{26}$$

where c_0 is a constant usually taken to be the Courant-Friedrichs-Lewy (CFL) number. Specifically, for the inviscid and viscous time step we used,

$$\Delta t_c = \frac{1}{\lambda_\xi + \lambda_\eta + \lambda_\zeta} \tag{27}$$

$$\Delta t_d = \frac{1}{K_t \frac{\gamma \mu}{\rho Pr} J^2 \left(S_\eta^2 S_\zeta^2 + S_\xi^2 S_\zeta^2 + S_\xi^2 S_\eta^2 \right)} \tag{28}$$

where γ is the specific heat ratio and,

$$S_\xi^2 = x_\xi^2 + y_\xi^2 + z_\xi^2, \quad S_\eta^2 = x_\eta^2 + y_\eta^2 + z_\eta^2, \quad S_\zeta^2 = x_\zeta^2 + y_\zeta^2 + z_\zeta^2, \tag{29}$$

K_t being a constant whose value has been set equal to 2.5 based on numerical experiments.

Residual Smoothing

An implicit smoothing of residuals is used to extend the stability limit and the robustness of the basic scheme. This technique was first introduced by Lerat in 1979 in conjunction with Lax-Wendroff type schemes. Later, in 1983, Jameson implemented it on the Runge-Kutta stepping scheme. In three dimensions we carried out the residual smoothing in the form,

$$\left(1-\beta_\xi \nabla_\xi \Delta_\xi\right)\left(1-\beta_\eta \nabla_\eta \Delta_\eta\right)\left(1-\beta_\zeta \nabla_\zeta \Delta_\zeta\right)\tilde{R}=R \tag{30}$$

where the residual R includes the contribution of the variable time step and is defined by (25) and $R;^{\sim}$ is the residual after a sequence of smoothing in the ξ, η, and ζ directions with coefficients β_ξ , β_η , and β_ζ. For viscous calculations on highly stretched meshes the variable coefficient formulations of Martinelli and Jameson (1988) and Swanson and Turkel (1987) have proven to be robust and reliable. In the present paper, the expression for the variable coefficients β of (30) has been modified to be used in three dimensions as follows,

$$\begin{aligned}
\beta_\xi &= MAX\left\{0,\frac{1}{4}\left[\left(\frac{CFL}{CFL^*}\frac{\lambda_\xi}{\lambda_\xi+\lambda_\eta+\lambda_\zeta}\Phi_\xi\right)^2-1\right]\right\}\\
\beta_\eta &= MAX\left\{0,\frac{1}{4}\left[\left(\frac{CFL}{CFL^*}\frac{\lambda_\eta}{\lambda_\xi+\lambda_\eta+\lambda_\zeta}\Phi_\eta\right)^2-1\right]\right\}\\
\beta_\zeta &= MAX\left\{0,\frac{1}{4}\left[\left(\frac{CFL}{CFL^*}\frac{\lambda_\zeta}{\lambda_\xi+\lambda_\eta+\lambda_\zeta}\Phi_\zeta\right)^2-1\right]\right\}
\end{aligned} \tag{31}$$

where the coefficients Φ_x, Φ_y and Φ_z are the ones defined in eqs. (19), and CFL, and CFL^* are the Courant numbers of the smoothed and unsmoothed scheme respectively. For the hybrid four-stage scheme we used $CFL=5$, and $CFL^*=2.5$.

Multigrid

This technique was developed in the beginning of the 1970s for the solution of elliptic problems (Brandt, 1979) and later was extended to time-dependent formulations (Ni, 1981, and Jameson, 1983). The basic idea is to introduce a sequence of coarser grids and to use them to speed up the propagation of the fine grid corrections, resulting in a faster expulsion of disturbances. In this work we used the Full Approximation Storage (FAS) schemes of Brandt (1979) and Jameson (1983).

Coarser, auxiliary meshes are obtained by doubling the mesh spacing and the solution is defined on them using a rule which conserves mass, momentum, and energy,

$$\left(J^{-1}Q^{(0)}\right)_{2h} = \Sigma\left(J^{-1}Q\right)_{h} \tag{32}$$

where the subscripts refer to the grid spacing, and the sum is over the eight cells which compose the $2h$ grid cell. Note that this definition coincides with the one used by Jameson when the reciprocal of the Jacobians are replaced with the cell volumes. To respect the fine grid approximation, forcing functions P are defined on the coarser grids and added to the governing equations. So, after the initialization of Q_{2h} using eq.(32), forcing functions P_{2h} are defined as,

$$P_{2h} = \Sigma R_h(Q_h) - R_{2h}(Q^{(0)}_{2h}) \tag{33}$$

and added to the residuals R_{2h} to obtain the value R^{*}_{2h} which is then used for the stepping scheme.

$$R^{*}_{2h} = R_{2h}(Q_{2h}) + P_{2h} \tag{34}$$

This procedure is repeated on a succession of coarser grids and the corrections computed on each coarse grid are transferred back to the finer one by bilinear interpolations.

A V-type cycle with subiterations is used as a multigrid strategy. The process is advanced from the fine grid to the coarser one without any intermediate interpolation, and when the coarser grid is reached, corrections are passed back. One Runge-Kutta step is performed on the h grid, two on the $2h$ grid, and three on all the coarser grids. It is our experience in cascade flow calculations that subiterations increase the robustness of the multigrid.

For viscous flows with very low Reynolds number or strong separation, it is important to compute the viscous terms on the coarse grids, too. The turbulent viscosity is evaluated only on the finest grid level and then interpolated on coarse grids.

On each grid, the boundary conditions are treated in the same way and updated at every Runge-Kutta stage. For economy, the artificial dissipation model is replaced on the coarse grids with constant coefficient second-order differences.

The interpolations of the corrections introduce high frequency errors. In order to prevent those errors from being reflected in the eddy viscosity, turbulent quantities are updated after performing the stepping on the fine grid. On coarse grids, the turbulent viscosity is evaluated by averaging the surrounding fine grid values.

Grid Refinement

A grid refinement strategy is used to provide a cost-effective initialization of the fine grid solution. This strategy is implemented in conjunction with multigrid to obtain a Full Multigrid (FMG) procedure. With the FMG method, the solution is initialized on a coarser grid of the basic grid sequence and iterated a prescribed number of cycles of the FAS scheme. The solution is then passed, by bilinear interpolations, onto the next, finer grid and the process is repeated until the finest grid level is reached. In the present paper we have introduced three levels of refinement with respectively two, three, and four grids.

COMPUTATIONAL GRID

The three-dimensional grids are obtained by stacking two dimensional grids generated on blade-to-blade surfaces at constant radii (ξ, η plane). In order to minimize the grid skewness, in the blade-to-blade projection, the grids structure can be chosen on the basis of the blade geometry and flow conditions. Turbine blades are generally characterized by blunt leading edge and high turn with a subsonic incoming flow in the relative plane. For these geometries, non-periodic C-type grids, have proven to be effective (e.g. Arnone et al., 1991, 1992). In the case of a compressor, and particularly for a fan, the leading aspect of the geometry is the high stagger and twist, while the leading edge is often quite sharp (fig. 1). In addition, the incoming flow in the relative plane can be supersonic for a large part of the blade span. As consequence, a C-type structure of the grid may smear too much of the bow shock away from the leading edge (i.e. Weber and Delaney, 1991). In the present work, a non-periodic H-type grid was implemented. The removal of mesh periodicity allow the grid to accommodate highly staggered airfoils with a low level of skewness. To minimize the undesired interaction between strong flow gradients and non-periodic boundaries the mesh correspondence is broken before the leading edge and on the wake, but not inside the blade channel. The inviscid grids are elliptically generated, controlling the grid spacing and orientation at the wall. Viscous blade-to-blade grids are then obtained from inviscid grids by adding lines near the wall with the desired spacing distribution.

For highly twisted blades, a low grid skewness in the various spanwise sections can also be maintained by adjusting the grid-point distributions on the suction and pressure sides of the blade.

In the spanwise direction (ζ) a standard H-type structure is used. Near the hub and tip endwalls, geometric stretching is used for a specified number of grid points, after which the spanwise spacing remains constant.

APPLICATION AND DISCUSSIONS

As validation of the procedure that has been described above, the TRAF3D code was used to study the NASA rotor 67 transonic fan. This first-stage rotor of a two-stage transonic fan was designed and tested with laser anemometer measurements at NASA Lewis (Pierzga and Wood, 1985). The rotor has *22* low aspect ratio (*1.56*) blades and was designed for a rotational speed of *16043* rpm, with a total pressure ratio of *1.63* and a mass flow of *33.25* kg/s. Experiments for simple blade-row code validation are available for the rotor without inlet guide vanes or downstream stators, and include detailed data near the peak efficiency and stall conditions. This rotor geometry has been recently proposed as an AGARD test case (Fottner, 1990) and several authors (Adamczyk et al. 1991, Chima, 1991, Hah and Reid, 1992, Jennions and Turner, 1992) have computed this geometry trying to understand the complex nature of transonic rotor flows. Therefore theoretical predictions from different codes are also available in the bibliography for comparisons and discussions.

A three-dimensional view of an inviscid grid for the rotor is given in fig. 1. In previous works by the author (Arnone et al., 1991, 1992), a two- and three-dimensional grid dependency study was carried out in order to figure out the mesh requirements necessary to obtain a space-converged calculation, especially for viscous details such as losses, skin friction and heat transfer. Those results can be extrapolated to the case of rotating blade passages. Using the algebraic turbulence model of Baldwin and Lomax (1978), a y^+ at the wall of about four, with a Reynolds number of about one million, gives satisfactory results unless heat transfer details are needed. This y^+ value was achieved with a mesh spacing at the wall in the blade-to-blade direction of 2×10^{-4} times the hub axial-chord. In the spanwise direction, due to the relatively thick inlet boundary layer, the mesh spacing at the wall was fixed at 1×10^{-3} times the hub axial-chord. One hundred thirty-seven points were used in the streamwise direction and *49* in the blade-to-blade and hub-to-tip directions. Sixty-five points were located on the suction and pressure side of the airfoil. In the spanwise direction, four cells lie inside the clearance region. Three grid sections at *70%*, *30%*, and *10%* of the span from the shroud, are shown in fig. 2(b), (c), and (d), respectively. Figure 2 (a) gives a meridional view of the grid.

Following the approach suggested by Pierzga and Wood (1985) the comparison between calculations and experiments is carried out using the mass flow rate nondimensionalized with the choke flow rate as equivalence criteria. However, good agreement was also found in terms of absolute quantities. The TRAF3D predicts *34.5* kg/s while *34.96* kg/s was the measured one. This underestimation of the choke flow rate of about *1.3*% agrees with the viscous prediction of Chima (1991) and Jennions and Turner (1992). The peak efficiency and near stall conditions correspond to a nondimensional flow rate of *.989* and *.924*, respectively.

The inlet boundary layer in the endwall region is accounted for by giving a total pressure profile. The thickness of the boundary layer is taken from experiments and the *1/7* power law velocity profile is used to estimate the distribution of total pressure. The core flow is assumed uniform.

The convergence of the root mean square of the norm of residuals is given in fig. 3. This calculation refers to the near-peak efficiency condition, and requires about *35* minutes on the NASA Lewis Cray Y-MP to achieve a four decades' reduction in the residuals and corresponds to *100* multigrid cycles on the finest grid level using four grids. More than *35* minutes were needed only for solutions close to the stall condition. The global mass flow error has always been found to be less then 10^{-3}.

Calculations were performed for *13* different values of the nondimensional flow rate in order reproduce the operating characteristics of the rotor at the design speed. Results are summarized in fig. 4 in terms of rotor adiabatic efficiency and rotor total pressure ratio. A nondimensional value of the mass flow rate equal to about *.91* was the smaller value for which a steady solution was obtained. Further increase in the exit pressure would produce tip stall. The prediction of the rotor efficiency is quite good and agrees with the indication of Jennions and Turner (1992) in the fact that the abrupt decrease going from peak efficiency to stall conditions is smoothed out in the calculations. The peak efficiency is predicted at a slightly lower mass flow rate. Some underestimation in the total pressure ratio across the rotor should be noticed, but it seems to be evident only when approaching the stall condition. It is believed that the following aspects could be investigated in order understand and/or address this problem:

- the distribution of the inlet boundary layer has been modelled only in terms of boundary layer thickness while experiments also show some gradients in the inviscid core of the inlet flow.
- the Baldwin-Lomax turbulence model is not very effective for transonic flow with strong adverse pressure gradients (Dawes, 1990).
- measurements of the machine geometry while running have shown some deformation not included in the present calculations (Fottner, 1990).
- the tip clearance model which has been used is quite simple and clearance flow becomes important when the stall condition is approached (Adamczyk et al., 1991, and Jennions and Turner, 1992).

The quality of the computed solutions is evaluated by comparing the spanwise distribution of circumferential energy-averaged thermodynamic quantities downstream of the rotor to experiments. The predicted distribution of static pressure, flow angle, total pressure, and total temperature at the rotor exit is compared to experiments in figs. 5 and 6 for conditions near peak efficiency and stall respectively. The agreement is good on the whole. The radial distribution of the static pressure is well reproduced (see figs. 5 (a) and 6 (a)), which indicates a good estimation of the global losses. The exit angle is up to five degrees off in the central part of the blade span (figs. 5 (b) and 6 (b)), but this agrees with the calculations of Chima (1991) and Jennions and Turner (1992). From the plots of total pressure and total temperature of figs. 5 and 6 (c) and (d) we can see that the overall prediction of the rotor characteristic is well reproduced.

As well known, the flow pattern inside a rotor like the NASA 67 transonic fan is very complicated and characterized by effects such as shock-boundary layer interaction, clearance flow, and three-dimensional separation with vortices roll up. One attempt at interpreting the structure of the computed flow field can be analyzing the relative flow on blade-to-blade and meridional surfaces. Pictures of the limiting streamlines inside the boundary layer can be obtained by means of particle traces.

Blade-to-blade flow

Figures 7 and 8 report the computed and measured relative Mach number contours at three different locations of the blade span. The agreement with experiments is qualitatively good and the bow shock is not too smeared away from the leading edge. It is also interesting to notice that those contours agree very well with the ones obtained by Jennions and Turner (1991) using a two-equation model for the turbulence closure.

Near peak efficiency, the shock system has a lambda structure with a bow shock. The passage shock crosses the blade channel and involves about 30% of the upper part of the airfoil (see figs. 7, and also 10, and 11). Approaching the stall condition (fig. 8) the passage shock moves upstream and stands in front of the blade so that the airfoil pressure side is no longer intercepted (see also figs. 12 and 13).

Blade surface flow pattern

Pressure distribution and a restriction of the particle traces close to the airfoil surface are used to interpret the flow pattern inside the blade boundary layer. A schematic of this structure for the peak efficiency condition is depicted in fig. 9. As discussed by Weber and Delaney (1991) and Hah and Reid (1991), most of the separation and outward flow is observed on the suction side of the blade. The passage shock is quite strong in the upper part of the rotor and the losses in axial momentum result in a rapid turn toward the shroud. The separation due to shock-boundary layer interaction is evident in figs. 10 and 11. Separation lines are characterized by flows going toward the line, while where the flow reattaches, the particle traces look like they are going away from the line (see. fig. 9). Such a situation is very clear in figs. 10 (c) and 13 (d). The passage shock also induces separation on the blade pressure side but only in the very upper part of the airfoil. The blow up of fig. 10 (c) shows the abrupt radial migration with separation and reattachment.

In the central part of the blade span, the passage shock loses intensity and the flow lift off is mostly related to the adverse pressure gradient in the axial direction. Eventually, near the trailing edge, the flow separates on the suction side (see fig. 11(b)).

Close to the blade root, the flow is strongly influenced by a vortex roll up on the leading edge. As also pointed out by Chima (1991), particles undergo a high relative incidence close to the hub, which causes the low-momentum fluid to separate and migrate radially outward (see figs. 10 (b) and 11 (b)).

In accordance with the calculations of Weber and Delaney (1991), Chima (1991), and Jennions and Turner (1991), a separation bubble is observed on the blade suction side near the hub (figs. 9, 11 (b), and 13 (d)).

The flow structure of the near-stall operating condition is qualitatively similar to the peak efficiency one previously discussed. Now the passage shock has moved upstream and the pressure side is shock free (fig. 12 (a)) with basically no radial flow mixing (fig. 12 (b)). On the contrary, on the suction side, the shock involves most of the blade span (fig. 13 (a)) and induces a strong outward flow with very clear separation and reattachment lines (fig. 13 (d)). The vortex roll up on the pressure side of fig. 10 (d) has now moved upstream and stands in front of the blade leading edge (fig. 13 (c)). The separation bubble on the suction side near the hub looks slightly smaller. On the shroud, the bow shock interacts with the casing boundary layer and the flow separates as depicted in fig. 13 (b).

Clearance flow pattern

A picture of the clearance flow pattern is obtained by plotting the relative Mach number contours and a restriction of the particle traces on a blade-to-blade surface midway between the blade tip and the casing. Once again the flow structure looks very similar to the one computed by Jennions and Turner (1991).

The TRAF3D code predicts two tip vortices which intersect before mid channel. At peak efficiency (fig. 14 (a) and (b)), the shock system still shows a lambda structure and interacts with the tip vortices. A first vortex is observed close to the leading edge and a second leakage vortex forms at an axial location just after the pressure side shock. The two vortices sum up before crossing the passage shock as shown in fig. 14. When approaching the stall condition there is interaction between the leading edge shock separation and the leading edge vortex (Adamczyk at. al (1991), and Jennions and Turner (1991)). The leading edge vortex is now associated with the casing separation of the bow shock, while the leakage vortex has moved upstream. The two vortices interact very soon while going towards the pressure side of the next consecutive blade (fig. 5(b) and (c). Figure 15 (d) indicates a strong link between the shock system and the tip vortices for this flow condition.

Hub endwall flow pattern

Particle traces in the hub boundary layer are reported for completeness in figs. 16 and 17. The high angle of attack experienced by the flow in this region and previously discussed is evident. The separation bubble close to the trailing edge causes a easily visible lack of particles, which, when injected close to the blade, roll up radially.

CONCLUSIONS

The central-difference, finite-volume scheme with eigenvalues scaling for artificial dissipation terms, variable-coefficient implicit smoothing, and full multigrid has been extended to predict three-dimensional rotating blade passages. The procedure has been validate by comparing it with experiment for the NASA rotor 67 in a wide range of mass flow rate. With these accelerating strategies, detailed three-dimensional viscous solutions can be obtained for a reasonable fine grid in about half an hour on a modern supercomputer.

ACKNOWLEDGEMENTS

The author would like to express his gratitude to ICOMP and NASA for providing computer time for this work. Thanks are also due to Prof. Sergio S. Stecco of the University of Florence, for encouraging this work.

REFERENCES

Adamczyk, J. J., Celestina, M. L., Beach, T. A., and Barnett, M.,1990, "Simulation of Three-Dimensional Viscous Flow Within a Multistage Turbine," *Transactions of the ASME*, Vol. 112, July 1990, pp. 370-376.

Adamczyk, J. J., Celestina, M. L., and Greitzer, E. M., 1991, "The Rule of Tip Clearance in High-Speed Fan Stall," paper 91-GT-83.

Arnone, A., and Swanson, R. C., 1988 " A Navier-Stokes Solver for Cascade Flows, " NASA CR No. 181682.

Arnone, A., Liou, M.-S., and Povinelli, L. A.,1991, " Multigrid Calculation of Three-Dimensional Viscous Cascade Flows, " AIAA paper 91-3238.

Arnone, A., Liou, M.-S., and Povinelli, L. A.,1992, "Navier-Stokes Solution of Transonic Cascade Flow Using Non-Periodic C-Type Grids, " *Journal of Propulsion and Power*, vol. 8, n. 2, March-April 1992, pp. 410-417.

Baldwin, B. S., and Lomax, H., 1978 "Thin Layer Approximation and Algebraic Model for Separated Turbulent Flows, " AIAA paper 78-257.

Brandt, A., 1979 " Multi-Level Adaptive Computations in Fluid Dynamics, " AIAA paper 79-1455.

Chima, R. V., and Yokota, J. W., 1988 "Numerical Analysis of Three-Dimensional Viscous Internal Flows," NASA TM 100878.

Chima, R. V., 1991, " Viscous Three-Dimensional Calculations of Transonic Fan Performance, " AGARD 77 th Symposium on CFD Techniques for Propulsion Applications, Paper No. 21.

Choi, D., and Knight, C. J., 1988 " Computation of Three-Dimensional Viscous Liner Cascade Flows, " *AIAA Journal*, Vol. 26, No. 12, December, pp. 1477-1482.

Davis, R. L., Hobbs, D. E., and Weingold, H. D., 1988, " Prediction of Compressor Cascade Performance Using a Navier-Stokes Technique," *ASME Journal of Turbomachinery*, Vol. 110, pp. 520-531.

Dawes, W. N., 1990, " A Comparison of Zero and One Equation Turbulence Modelling for Turbomachinery Calculations, " ASME 90-GT-303.

Dawes, N. W., 1991 " The Simulation of Three-Dimensional Viscous Flow in Turbomachinery Geometries Using a Solution-Adaptive Unstructured Mesh Methodology, " ASME paper 91-GT-124.

Fottner, L., 1990, " Test Case for Computation of Internal Flows in Aero Engine Components," Propulsion and Energetic Panel Working Group 18, AGARD-AR-275.

Hah, C., 1989 " Numerical Study of Three-Dimensional Flow and Heat Transfer Near the Endwall of a Turbine Blade Row, " AIAA paper 89-1689,.

Hah, C., and Reid, L., 1992 " A Viscous Flow Study of Shock-Boundary Layer Interaction, Radial Transport, and Wake Development in a Transonic Compressor, " ASME 90-GT-303.

Holmes, D., G., and Tong, S., S., 1985, " A Three-Dimensional Euler Solver for Turbomachinery Blade Rows," Journal of Engineering for Gas Turbines and Power, April 1985, Vol. 107, pp. 258-264

Jameson, A., Schmidt, W., and Turkel, E., 1981 " Numerical Solutions of the Euler Equations by Finite Volume Methods Using Runge-Kutta Time-Stepping Schemes, " AIAA paper 81-1259.

Jameson, A., 1983 " The Evolution of Computational Methods in Aerodynamics, " *J. Appl. Mech.*, Vol. 50.

Jameson, A., 1983 " Transonic Flow Calculations, " MAE Report 1651, MAE Department, Princeton University.

Jennions, I. K., and Turner, M. G., 1992 " Three-Dimensional Navier-Stokes Computations of Transonic Fan Flow Using an Explicit Flow Solver and an Implicit κ-ε Solver, " ASME paper 92-GT-309.

Lerat, A., 1979 " Une Classe de Schemas aux Differences Implicites Pour les Systemes Hyperboliques de Lois de Conservation, "*Comptes Rendus Acad. Sciences Paris*, Vol. 288 A.

Martinelli, L. and Jameson, A., 1988 " Validation of a Multigrid Method for the Reynolds Averaged Equations, " AIAA paper 88-0414.

Nakahashi, K., Nozaki, O., Kikuchi, K., and Tamura, A., 1989 " Navier-Stokes Computations of Two- and Three- Dimensional Cascade Flowfields, " *AIAA Journal of Propulsion and Power*, Vol. 5, No. 3, May-June, pp. 320-326.

Ni, R-H, 1981 " A Multiple-Grid Scheme for Solving the Euler Equations, " AIAA paper 81-1025.

Pierzga, M. J., and Wood, J. R., 1985, " Investigation of the Three-Dimensional Flow Field Within a Transonic Fan Rotor: Experiment and Analysis, " *Transaction of the ASME*, vol. 107, April 1985, pp. 436-449.

Pulliam, T. H., 1986 " Artificial Dissipation Models for the Euler Equations, " *AIAA Journal*, Vol. 24, No. 12, December, pp. 1931-1940.

Rai, M. M., 1987, " Unsteady Three-Dimensional Navier-Stokes Simulations of Rotor Stator Interactions, " AIAA paper 87-2058.

Rao, K. V., and Delaney, R. A., 1990 " Investigation of Unsteady Flow Through a Transonic Turbine Stage, Part I, Analysis," AIAA paper 90-2408.

Subramanian, S. V., and Bozzola, R., 1987 " Numerical Simulation of Three-Dimensional Flow Fields in Turbomachinery Blade Rows Using the Compressible Navier-Stokes Equations, " AIAA paper 87-1314.

Swanson, R. C., and Turkel, E., 1987 " Artificial Dissipation and Central Difference Schemes for the Euler and Navier-Stokes Equations., " AIAA paper 87-1107.

Weber, K. F., and Delaney, R. A., 1991 " Viscous Analysis of Three-Dimensional Turbomachinery Flows on Body Conforming Grids Using an Implicit Solver," ASME paper 91-GT-205.

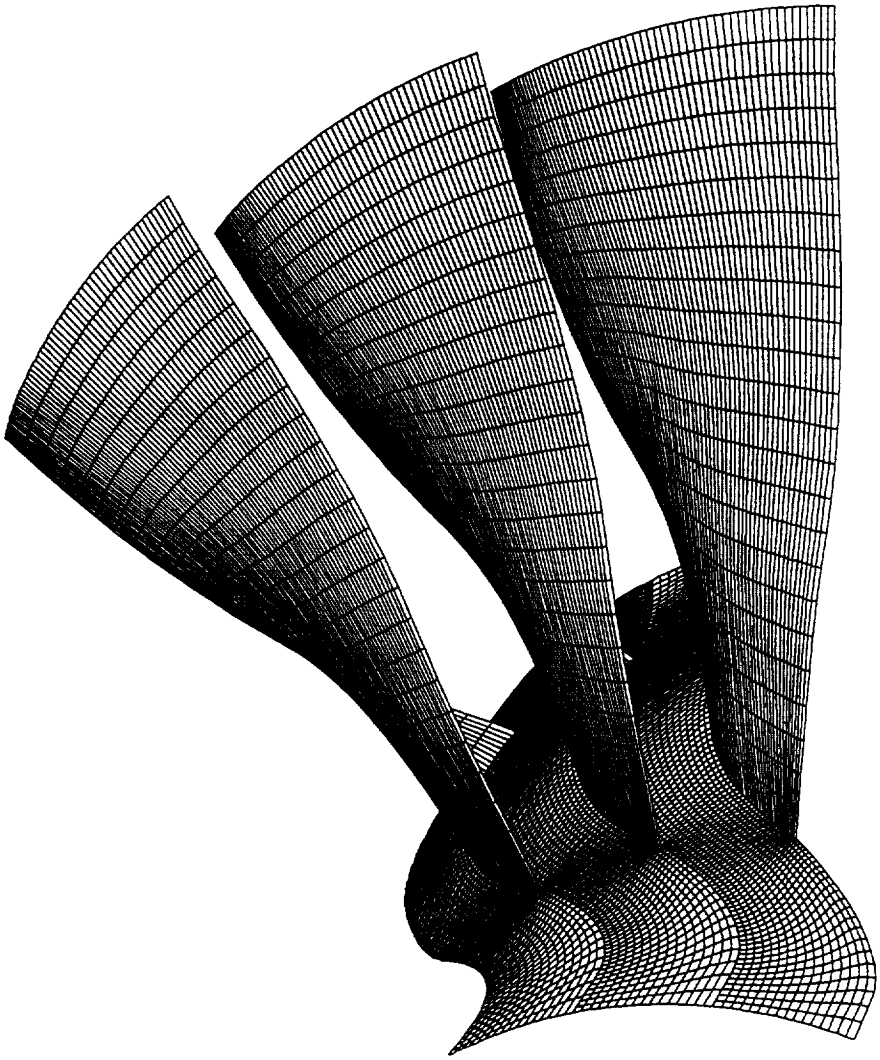

Fig. 1 Three-dimensional inviscid grid for the NASA rotor 67 transonic fan.

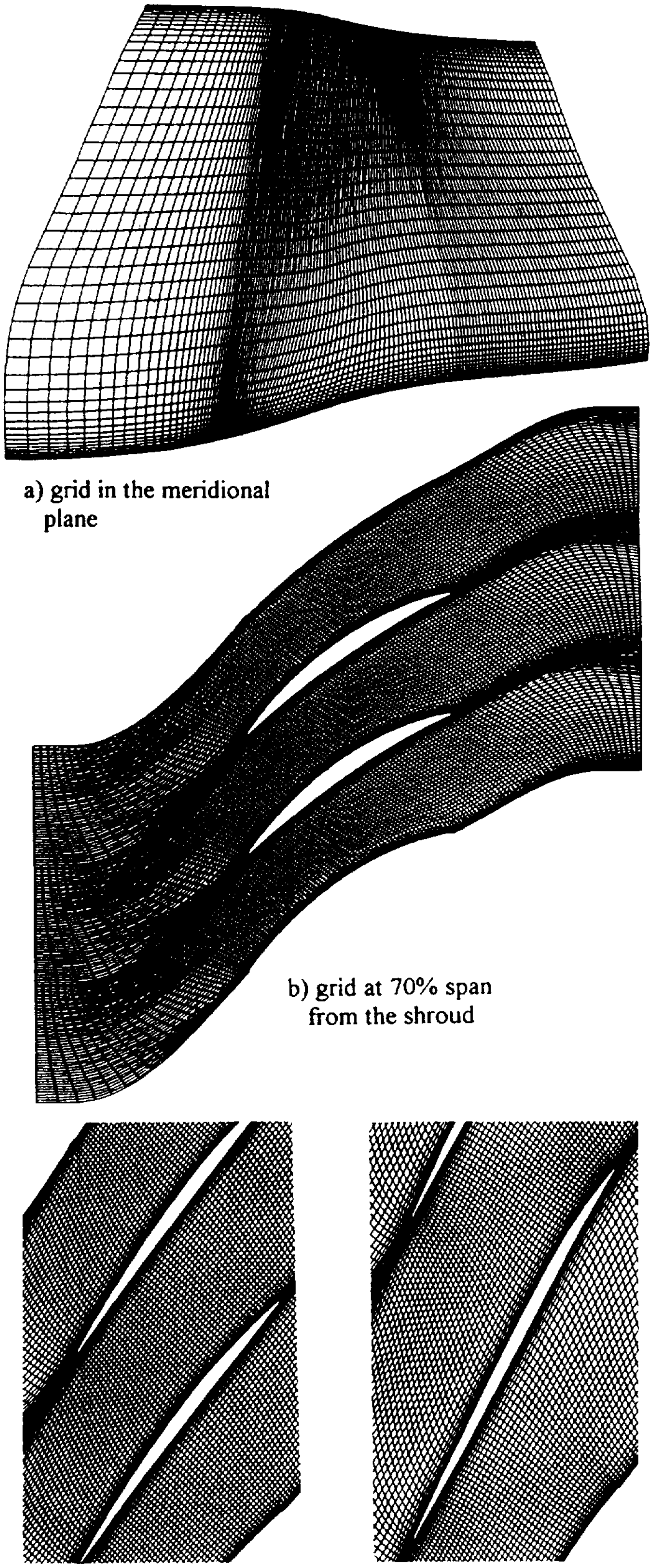

a) grid in the meridional plane

b) grid at 70% span from the shroud

c) grid at 30% span from the shroud

d) grid at 10% span from the shroud

Fig. 2 137x49x49 viscous grid for the NASA rotor 67 transonic fan.

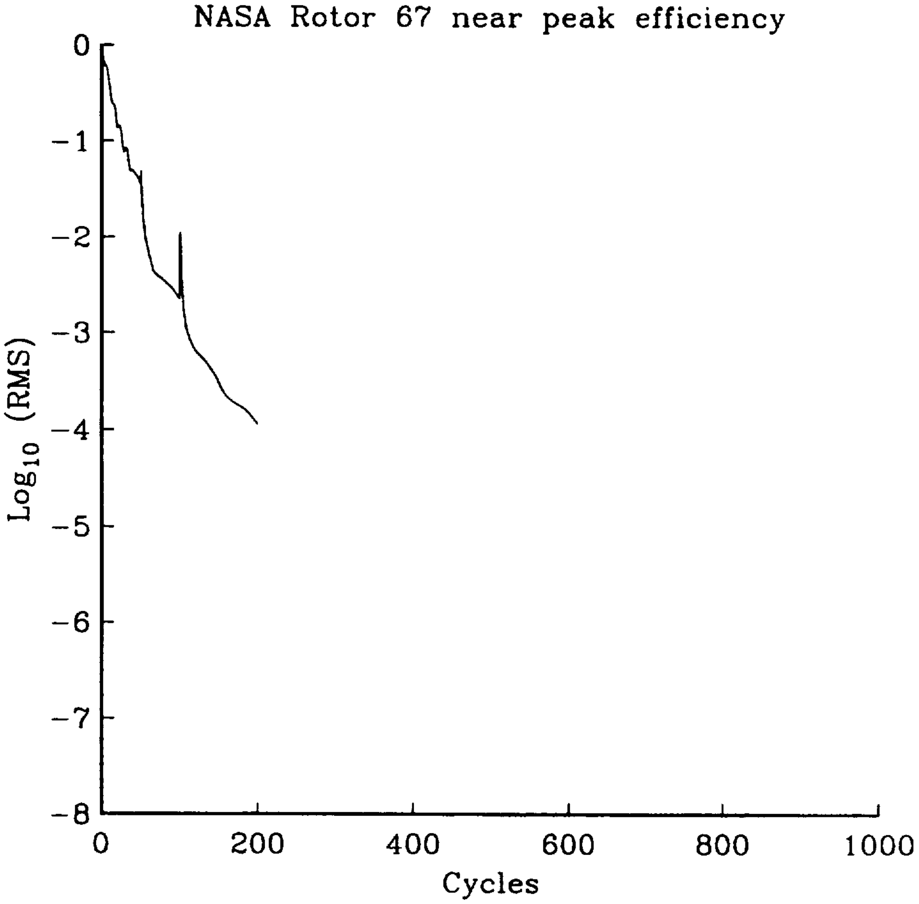

Fig. 3 Convergence history for the near peak efficiency condition (NASA rotor 67 transonic fan).

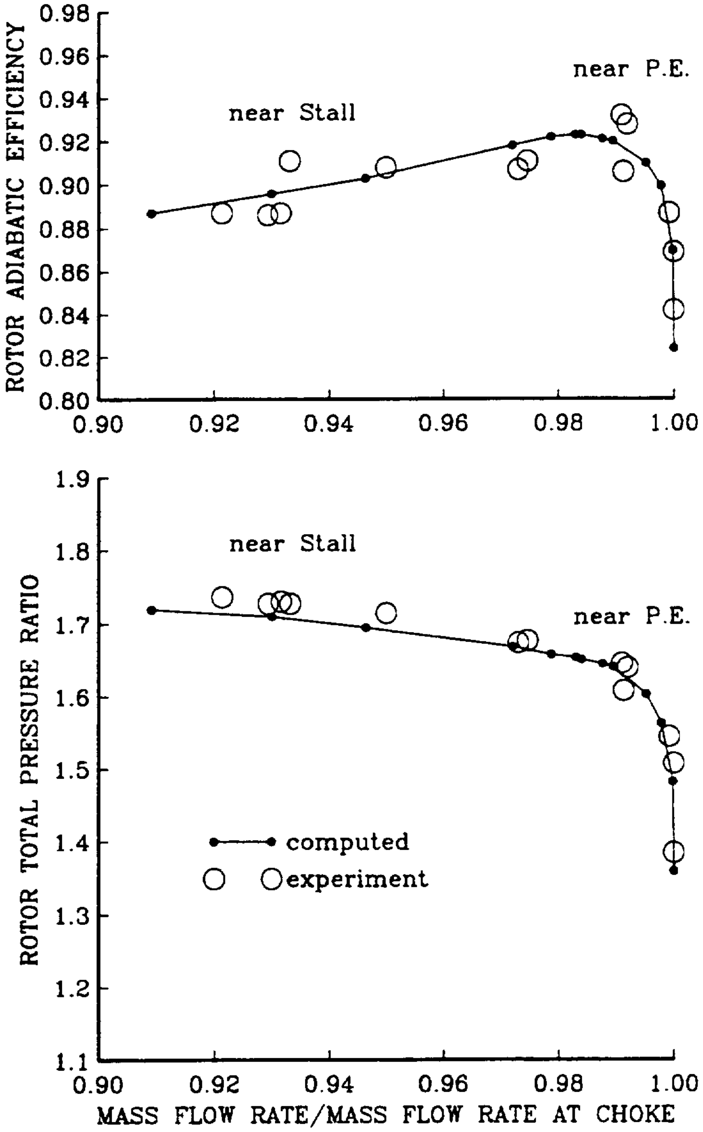

Fig. 4 NASA rotor 67 performance at design speed.

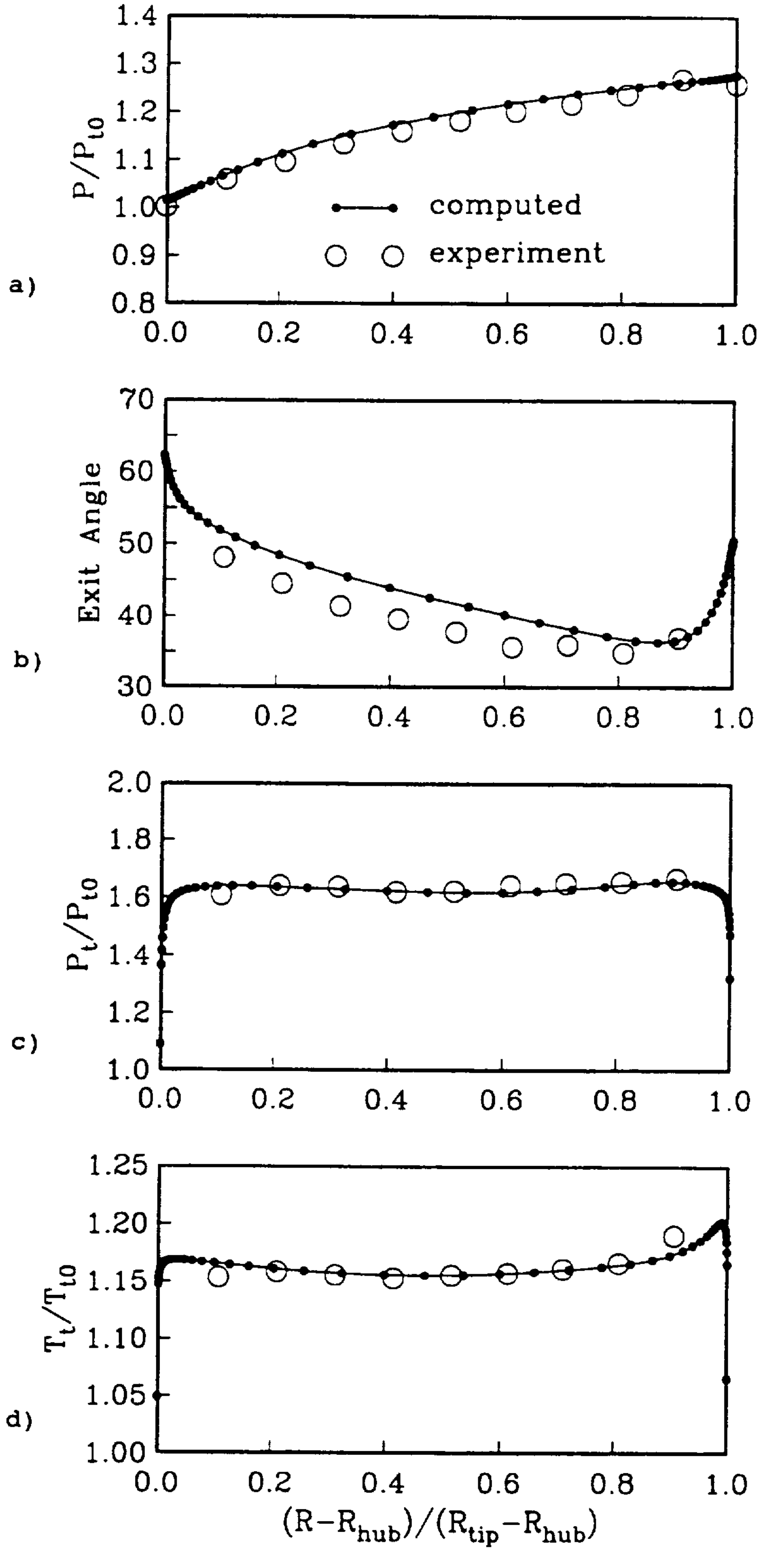

Fig. 5 Predicted and measured exit survey data near peak efficiency (NASA rotor 67).

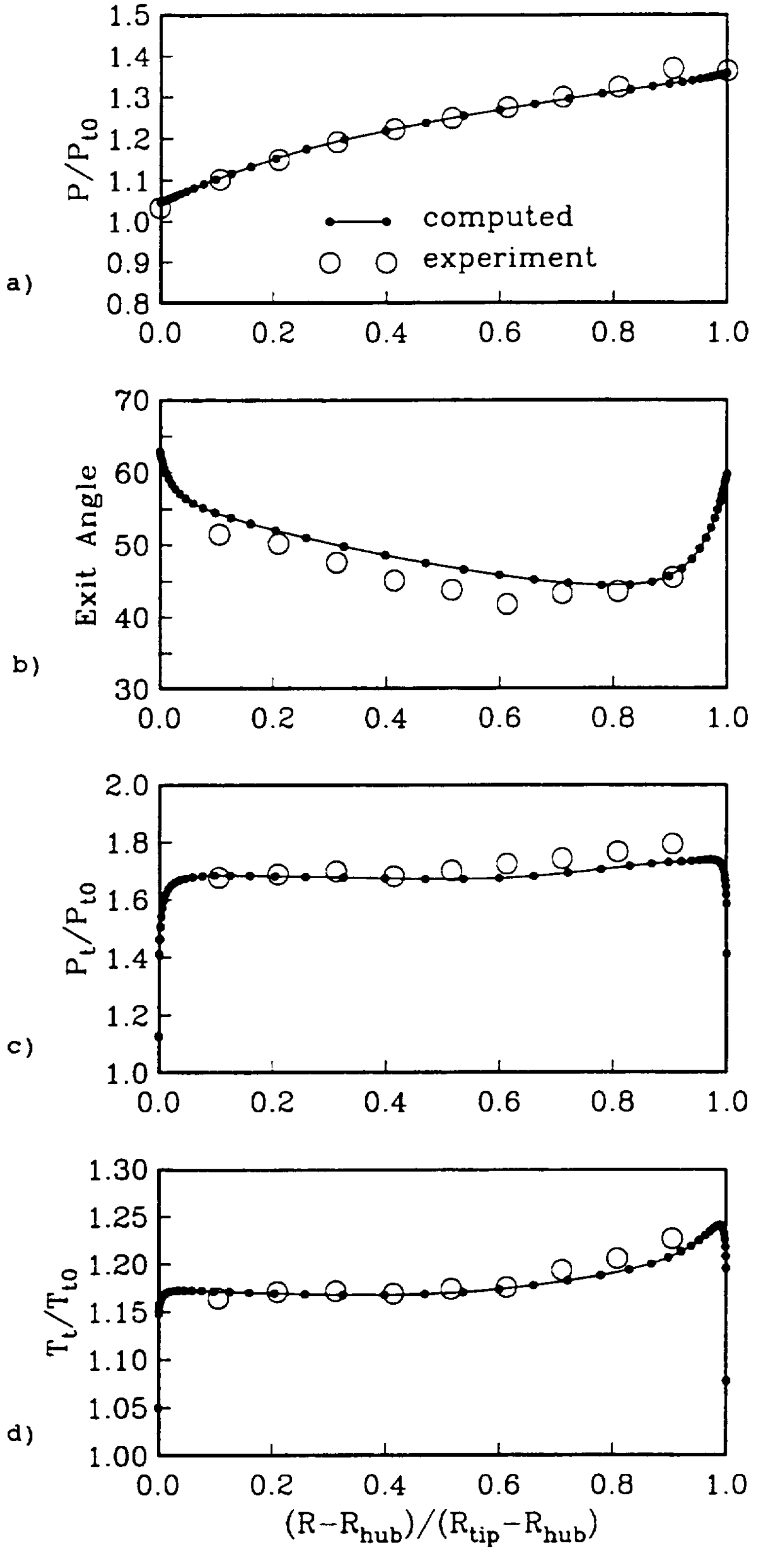

Fig. 6 Predicted and measured exit survey data near stall (NASA rotor 67).

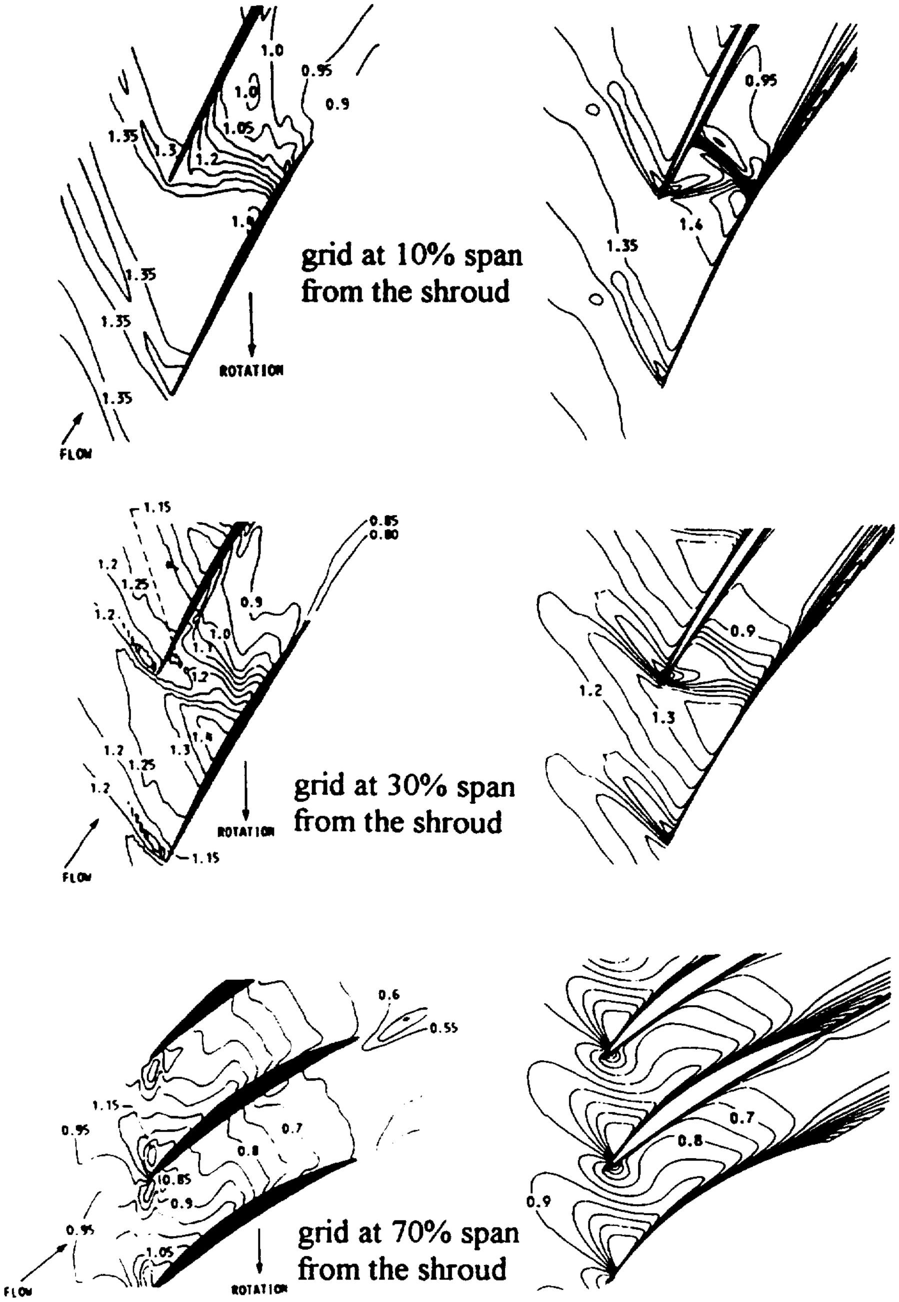

grid at 10% span from the shroud

grid at 30% span from the shroud

grid at 70% span from the shroud

Fig. 7 Measured (left) and predicted (right) relative Mach number contours near peak efficiency (NASA rotor 67).

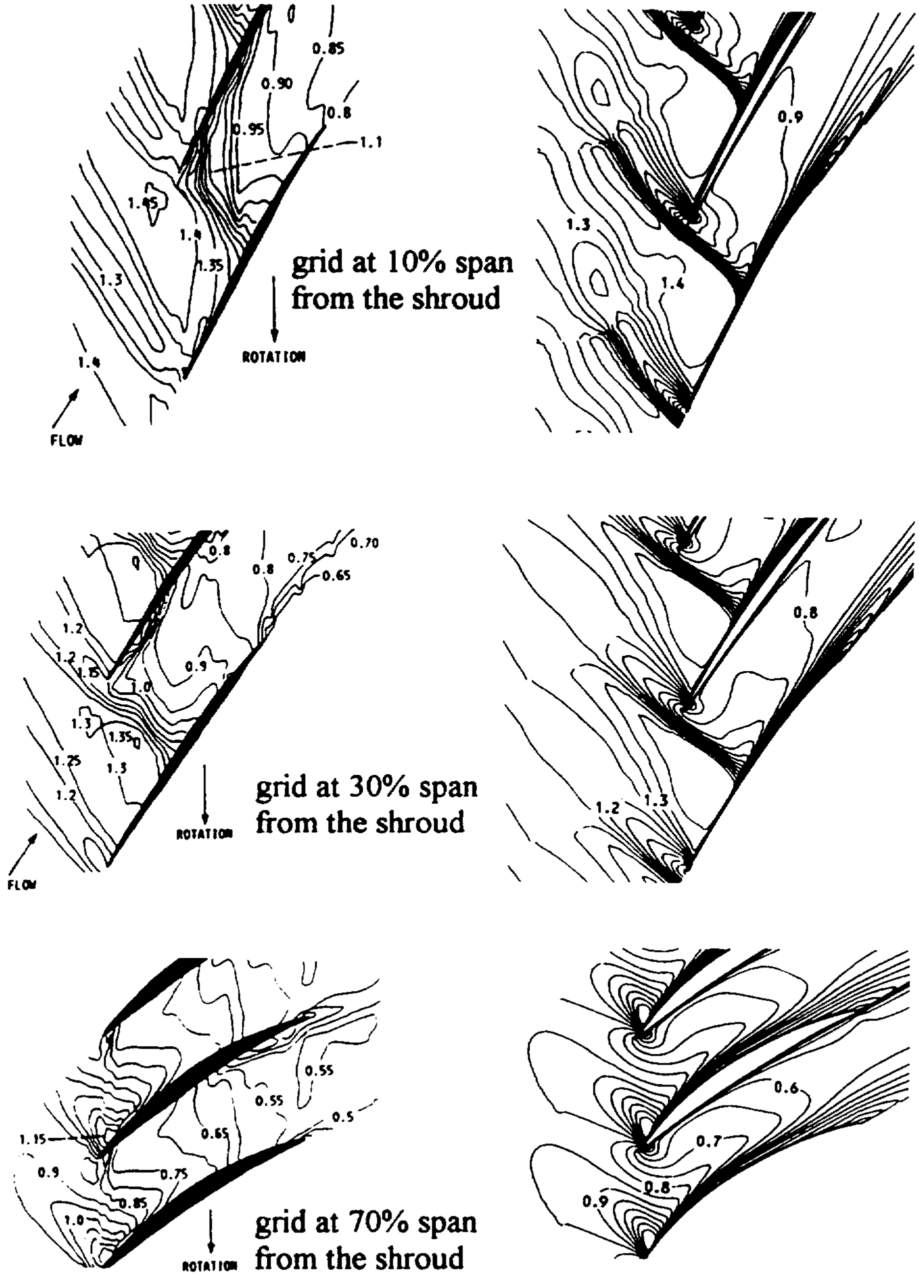

Fig. 8 Measured (left) and predicted (right) relative Mach number contours near stall (NASA rotor 67).

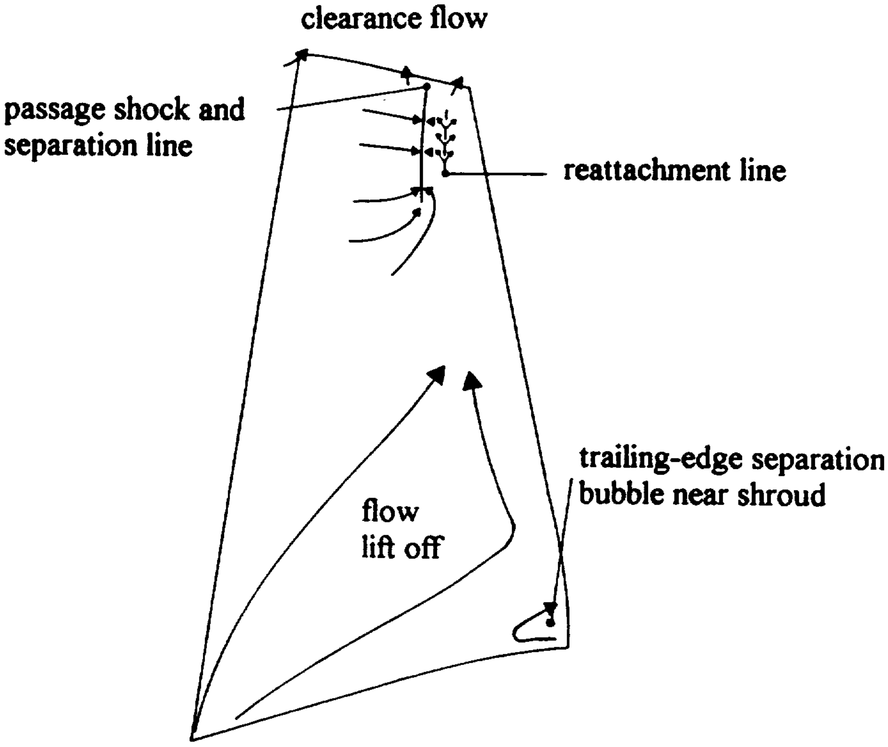

Fig. 9 Schematic of the suction side boundary-layer flow structure near peak efficiency (NASA rotor 67).

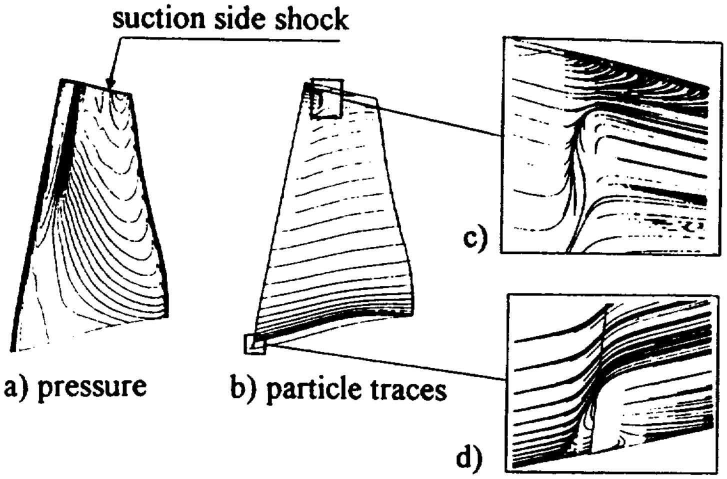

a) pressure b) particle traces

Fig. 10 Pressure contours and particle traces close to the blade pressure side near peak efficiency (NASA rotor 67).

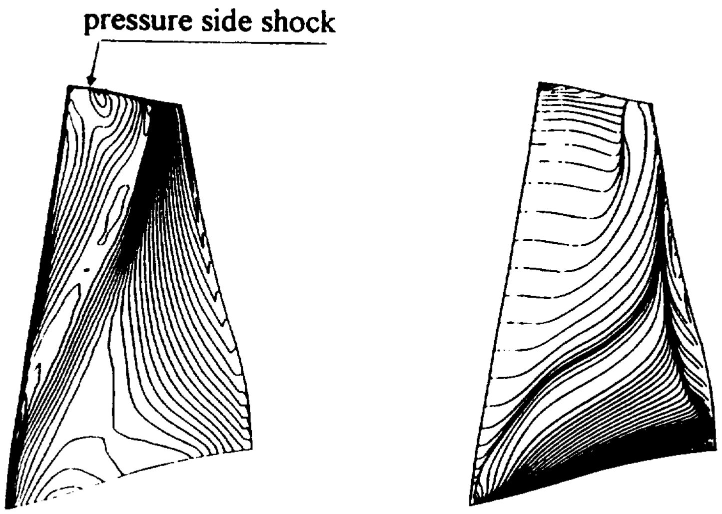

a) pressure

b) particle traces

Fig. 11 Pressure contours and particle traces close to the blade suction side near peak efficiency (NASA rotor 67).

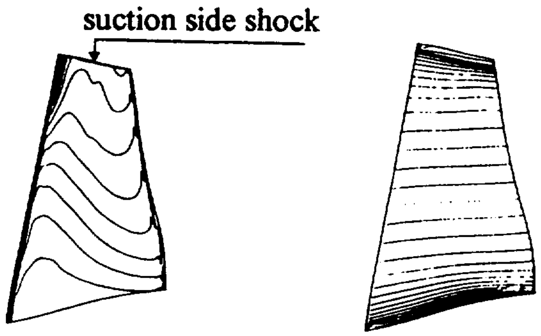

a) pressure

b) particle traces

Fig. 12 Pressure contours and particle traces close to the blade pressure side near stall (NASA rotor 67).

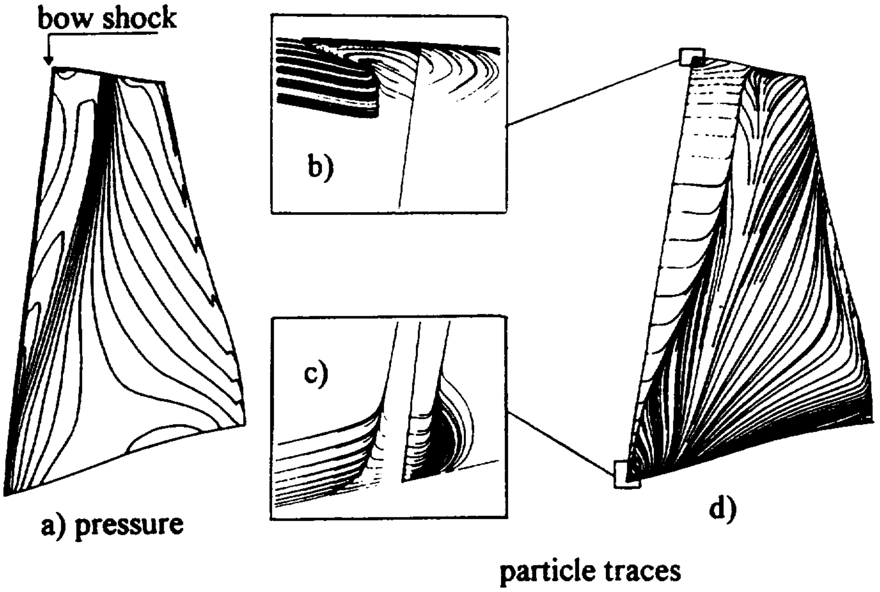

Fig. 13 Pressure contours and particle traces close to the blade suction side near stall (NASA rotor 67).

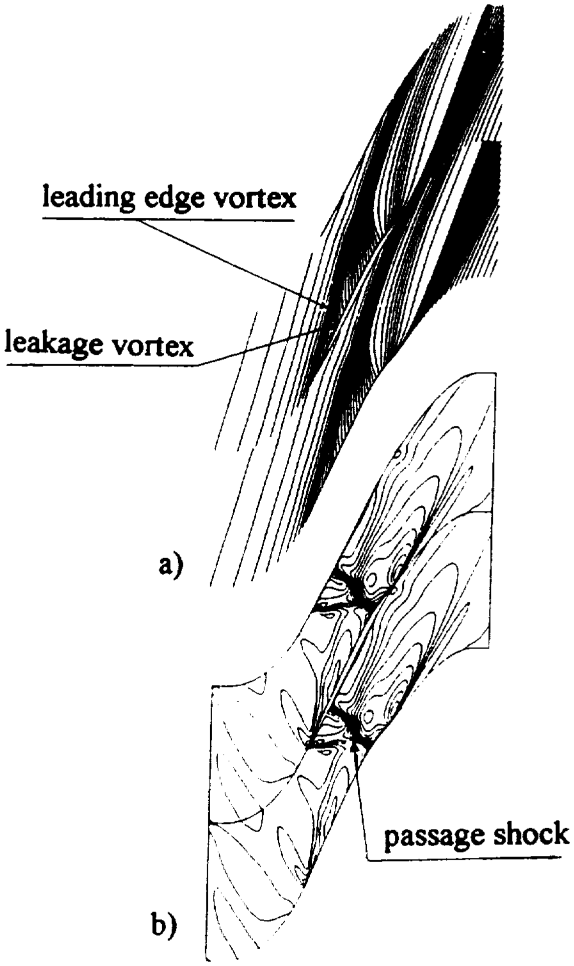

Fig. 14 Particle traces and relative Mach number contours in the clearance region near peak efficiency (NASA rotor 67).

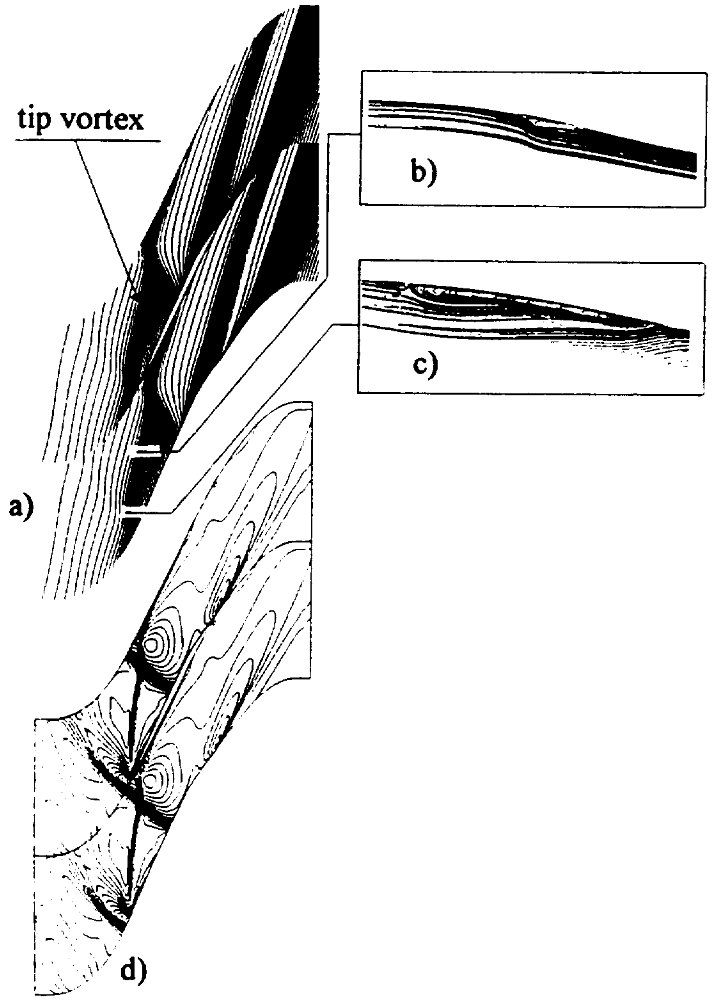

Fig. 15 Particle traces and relative Mach number contours in the clearance region near stall (NASA rotor 67).

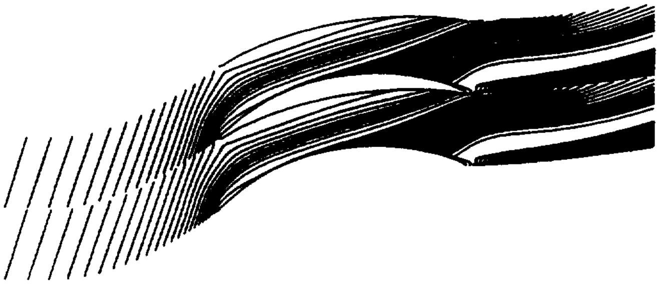

Fig. 16 Particle traces close to the hub endwall near peak efficiency (NASA rotor 67).

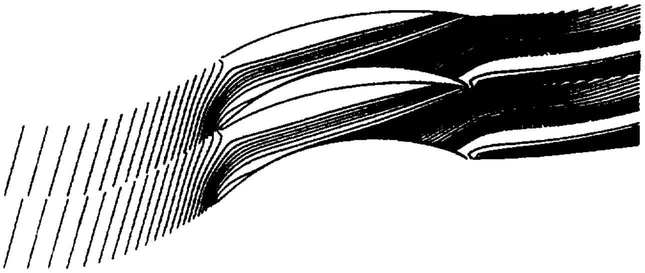

Fig. 17 Particle traces close to the hub endwall near stall (NASA rotor 67).

REPORT DOCUMENTATION PAGE	*Form Approved* *OMB No. 0704-0188*

1. AGENCY USE ONLY (*Leave blank*)	**2. REPORT DATE** July 1993	**3. REPORT TYPE AND DATES COVERED** Technical Memorandum

4. TITLE AND SUBTITLE

Viscous Analysis of Three-Dimensional Rotor Flows Using a Multigrid Method

5. FUNDING NUMBERS

WU-505-90-5K

6. AUTHOR(S)

A. Arnone

7. PERFORMING ORGANIZATION NAME(S) AND ADDRESS(ES)

National Aeronautics and Space Administration
Lewis Research Center
Cleveland, Ohio 44135-3191

8. PERFORMING ORGANIZATION REPORT NUMBER

E-7993

9. SPONSORING/MONITORING AGENCY NAME(S) AND ADDRESS(ES)

National Aeronautics and Space Administration
Washington, D.C. 20546-0001

10. SPONSORING/MONITORING AGENCY REPORT NUMBER

NASA TM-106266
ICOMP-93-25

11. SUPPLEMENTARY NOTES

A. Arnone, Institute for Computational Mechanics in Propulsion, NASA Lewis Research Center and University of Florence, Department of Energy Engineering, Florence, Italy, (work funded under NASA Cooperative Agreement NCC3-233). ICOMP Program Director, Louis A. Povinelli, (216) 433-5818.

12a. DISTRIBUTION/AVAILABILITY STATEMENT

Unclassified - Unlimited
Subject Category 34

12b. DISTRIBUTION CODE

13. ABSTRACT ***(Maximum 200 words)***

A three-dimensional code for rotating blade-row flow analysis has been developed. The space discretization uses a cell-centered scheme with eigenvalues scaling for the artificial dissipation. The computational efficiency of a four-stage Runge-Kutta scheme is enhanced by using variable coefficients, implicit residual smoothing, and a full-multigrid method. An application is presented for the NASA rotor 67 transonic fan. Due to the blade stagger and twist, a zonal, non-periodic H-type grid is used to minimize the mesh skewness. The calculation is validated by comparing it with experiments in the range from the maximum flow rate to a near-stall condition. A detailed study of the flow structure near peak efficiency and near stall is presented by means of pressure distribution and particle traces inside boundary layers.

14. SUBJECT TERMS

Multigrid methods; 3-D rotor flow; Cascades; Navier-Stokes equations

15. NUMBER OF PAGES

36

16. PRICE CODE

A03

17. SECURITY CLASSIFICATION OF REPORT Unclassified	**18. SECURITY CLASSIFICATION OF THIS PAGE** Unclassified	**19. SECURITY CLASSIFICATION OF ABSTRACT** Unclassified	**20. LIMITATION OF ABSTRACT**

National Aeronautics and
Space Administration

Lewis Research Center
ICOMP (M.S. 5-3)
Cleveland, Ohio 44135